Poloidal Flux Profile Reconstruction From Pointwise Measurements via Extended Kalman Filtering in the DIII-D Tokamak

Hexiang Wang, Justin E. Barton and Eugenio Schuster

Abstract— The accuracy of the internal states of a tokamak, which usually cannot be measured directly, is of crucial importance for feedback control of the plasma dynamics. A first-principles-driven plasma response model could provide an estimation of the internal states given the boundary conditions on the magnetic axis and at plasma boundary. However, the estimation would highly depend on initial conditions, which may not always be known, disturbances, and non-modeled dynamics. In this work, a closed-loop state observer for the poloidal magnetic flux is proposed based on a very limited set of real-time measurements by following an Extended Kalman Filtering (EKF) approach. Comparisons between estimated and measured magnetic flux profiles are carried out for several discharges in the DIII-D tokamak. The experimental results illustrate the capability of the proposed observer in dealing with incorrect initial conditions and measurement noise.

I. INTRODUCTION

Nuclear fusion is the process by which two light nuclei fuse together to form one heavier nucleus. There is a mass fraction Δm that is converted into energy according to the mass-energy equivalence $\Delta E = \Delta m c^2$, where c is the speed of light in vacuum. In order for the fusion reaction to occur frequently enough, the nuclei must be heated to temperatures of about one hundred million degrees. At these temperatures, the reactants are in the plasma state and have enough kinetic energy to overcome the repelling electrostatic forces and fuse. One of the most promising approaches to nuclear fusion is magnetic confinement, where magnetic fields are used to confine the plasma. A common solution is to close the magnetic field lines in on themselves, forming a torus as shown in Fig. 1 and leading to a tokamak configuration. In a tokamak, the magnetic field lines follow a helical path through the torus, i.e. they curve around in the poloidal direction (B_θ) as well as in the toroidal direction (B_ϕ). Following any magnetic field line a number of times around the torus a closed flux tube is mapped, a so called magnetic-flux surface, which marks points of constant poloidal magnetic flux, Ψ [1]. A collection of such points along a plasma radial coordinate (ρ in Fig. 1) is called the poloidal magnetic flux profile.

Extensive research has been conducted to find high-performance operating scenarios characterized by a high fusion gain, good plasma confinement, plasma stability, and a noninductively driven plasma current with the goal of developing candidate scenarios for ITER [2]. A key property that is related to both the stability and performance of these advanced plasmas is the magnetic poloidal flux profile and its gradients. The design of control algorithms for the regulation of these profiles has recently attracted a great deal of attention [3]–[10].

Unfortunately, the values of several discharge parameters, including the magnetic poloidal flux profile, are not directly measured in tokamaks. However, these values can be reconstructed from magnetic field and flux measurements. Equilibrium codes, such as EFIT [11], calculate the distributions of magnetic poloidal flux and toroidal current density over the plasma and surrounding vacuum region that best fit, in a least square sense, the external and any available internal magnetic measurements, and that simultaneously satisfy the magneto-hydrodynamic equilibrium equation (Grad-Shafranov equation) [12]. Real-time versions of these equilibrium codes [13] play a crucial role in the feedback control of the plasma position, shape and internal profiles. However, the quality of the reconstruction depends strongly on the availability of internal measurements such as those provided by the Motional Stark Effect (MSE) diagnostic available in the DIII-D [14] tokamak, which gives a measure of the pitch angle of the plasma magnetic field.

In tokamaks where MSE diagnostics, or any other internal diagnostics, are not available, the plasma equilibrium reconstruction is poorly constrained by just external measurements and the estimation of the internal magnetic poloidal flux profile is not accurate. For these cases a state observer approach is proposed in this work. First, the first-principles physics model of the poloidal magnetic flux profile evolution in the tokamak is converted into a form suitable for control design. This is accomplished by combining the poloidal flux evolution model with simplified control-oriented versions of physics-based models of the electron density and temperature profiles, the plasma resistivity, and the noninductive current-drives, with emphasis on high performance, high confinement (H-mode) scenarios, thereby obtaining a first-principles-driven model [15]. Second, a state observer based on the Kalman filtering approach is proposed. An extended Kalman filter (EKF) is designed based on the first-principles-driven control-oriented model of magnetic poloidal flux profile. At each time instant, the nonlinear state equation is linearized around the state estimated at the previous time step. Kalman filtering has found some applications in plasma control, such as the estimation of induced vessel currents [16] or unknown plasma transport parameters [17]. Previous work in this area include the estimation of both the magnetic poloidal flux profile and the temperature profile from simulated data [18] assuming availability of internal profile measurements. In this work, on the contrary, MSE-constrained EFIT-reconstructed magnetic poloidal flux profiles from DIII-D are used to validate the observer-based profile estimation obtained from pointwise (not-internal) measurements at the boundaries.

The paper is organized as follows. The first-principles-driven control-oriented model of the poloidal magnetic flux and the numerical discretization method are introduced in Section II and Section III. The observability of the discretized system is discussed in Section IV. In Section V, an observer is designed based on the extended Kalman filter theory. Comparisons between experimentally reconstructed and observer-based estimated poloidal flux profiles are presented in Section VI to show the effectiveness of the observer. Conclusions and future work are discussed in Section VII.

II. POLOIDAL MAGNETIC FLUX MODEL

From Gauss's law for magnetism, $\nabla \cdot \bar{B} = 0$, we can write the magnetic field $\bar{B}$ as the curl of a vector potential, i.e., $\bar{B} = \nabla \times \bar{A}$. In cylindrical coordinates, $\bar{R} = (R, \phi, Z)$, we write the vector potential as $\bar{A} = (A_R, A_\phi, A_Z)$. Assuming an axisymmetric configuration ($\partial/\partial\phi = 0$), the magnetic field is written as

$$\bar{B} = (B_R, B_\phi, B_Z) = \left(-\frac{1}{R}\frac{\partial\psi}{\partial Z}, B_\phi, \frac{1}{R}\frac{\partial\psi}{\partial R} \right), \quad (1)$$

where we define the stream function $\psi(R, Z) = RA_\phi(R, Z)$. This quantity is closely related to the poloidal flux Ψ, i.e.,

$$\Psi = \int_S B_\theta \cdot dS = \int_0^{2\pi} d\phi \int_0^R RB_Z(R, Z)dR = 2\pi\psi, \quad (2)$$

where S denotes the surface normal to Z bounded by the toroidal ring passing through the point P in the (R, Z) cross section at which the poloidal flux is computed (see Fig. 1). The magnetic surface $\psi(\bar{R}) = constant$ is such that all magnetic lines of force lie upon on that surface, i.e., $\nabla\psi(\bar{R}) \cdot \bar{B} = 0$ on the magnetic surface. We let ρ be an arbitrary coordinate indexing the magnetic surfaces. Any quantity constant on each magnetic surface could be chosen as the variable ρ. We choose the mean effective minor radius of the magnetic surface as the variable ρ, i.e., $\pi B_{\phi,0}\rho^2 = \Phi$, where Φ is the toroidal magnetic flux and $B_{\phi,0}$ is the toroidal magnetic field at the major radius R_0 of the device. The normalized effective minor radius $\hat{\rho}$ is defined as $\hat{\rho} = \rho/\rho_b$, where ρ_b is the mean effective minor radius of the outermost closed magnetic flux surface. The configuration of typical tokamak magnetic flux surfaces is shown in Fig. 1.

A. Magnetic diffusion equation

The dynamics of the poloidal magnetic flux is governed by the magnetic-flux diffusion equation (MDE) [15],

$$\frac{\partial\psi}{\partial t} = \frac{\eta(T_e)}{\mu_0\rho_b^2\hat{F}^2}\frac{1}{\hat{\rho}}\frac{\partial}{\partial\hat{\rho}}\left(\hat{\rho}D_\psi\frac{\partial\psi}{\partial\hat{\rho}} \right) + R_0\hat{H}\eta(T_e)\frac{\langle\bar{j}_{NI}\cdot\bar{B}\rangle}{B_{\phi,0}}, \quad (3)$$

where t is the time, η is the plasma resistivity, T_e is the electron temperature, μ_0 is the vacuum permeability, $\bar{j}_{NI}$ is any source of noninductive current density, $\bar{B}$ is the magnetic field, $\langle\rangle$ denotes a flux-surface average, and $D_\psi(\hat{\rho}) = \hat{F}(\hat{\rho})\hat{G}(\hat{\rho})\hat{H}(\hat{\rho})$. The parameters $\hat{F}, \hat{G}, \hat{H}$ are geometric factors pertaining to the magnetic configuration
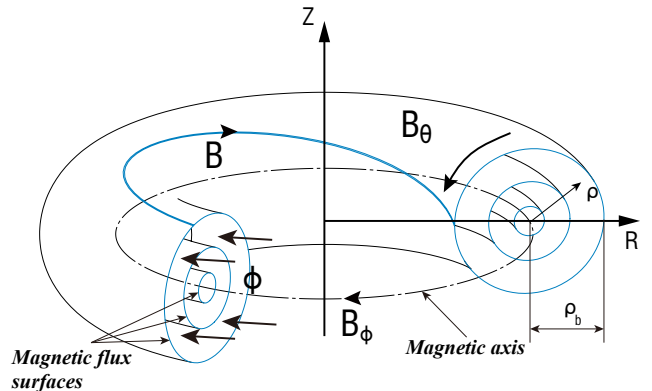

Fig. 1. Cross-section view of the magnetic flux surfaces in a tokamak. The limiting flux surface at the center of the plasma is called the magnetic axis. The coordinates (R, Z) define the radial and vertical dimensions in the poloidal plane of the tokamak. The poloidal (B_θ) and toroidal (B_ϕ) components of the magnetic field define helical paths around the torus. The toroidal magnetic field B_ϕ is the driver of the toroidal magnetic flux Φ.

of a particular plasma equilibrium. The boundary conditions are given by

$$\left.\frac{\partial\psi}{\partial\hat{\rho}}\right|_{\hat{\rho}=0} = 0 \qquad \left.\frac{\partial\psi}{\partial\hat{\rho}}\right|_{\hat{\rho}=1} = -\frac{\mu_0}{2\pi}\frac{R_0}{\hat{G}(1)\hat{H}(1)}I_p(t), \quad (4)$$

where $I_p(t)$ is the total plasma current.

B. Electron temperature modeling

The electron temperature T_e is modeled as

$$T_e(\hat{\rho}, t) = T_e^{profile}(\hat{\rho})\frac{I_p(t)\sqrt{P_{tot}(t)}}{n_e(\hat{\rho}, t)}, \quad (5)$$

where $T_e^{profile}$ is a reference electron temperature profile and P_{tot} is the total power injected into the plasma. $T_e^{profile}$ is obtained by evaluating the experimental T_e at a reference time t_{rT_e}, i.e.

$$T_e^{profile}(\hat{\rho}) = \frac{T_e(\hat{\rho}, t_{rT_e})n_e(\hat{\rho}, t_{rT_e})}{I_p(t_{rT_e})\sqrt{P_{tot(t_{rT_e})}}}. \quad (6)$$

This model exploits the time scale separation between magnetic (ψ) and kinetic (T_e) variables in tokamaks. For current profile control purposes, any partial-differential-equation (PDE) model for the electron temperature (heat transport equation) can be reduced to an ordinary differential equation (ODE) by following a singular perturbation approach. Its approximate solution is assumed to adopt the form in (5).

C. Electron density modeling

The electron density n_e is modeled as

$$n_e(\hat{\rho}, t) = n_e^{prof}(\hat{\rho})\bar{n}_e(t), \quad (7)$$

where n_e^{prof} is a reference electron density profile obtained at reference time t_{rn_e}, i.e., $n_e^{prof}(\hat{\rho}) = n_e(\hat{\rho}, t_{rn_e})/\bar{n}_e(t_{rn_e})$, and $\bar{n}_e(t)$ is the line-averaged electron density, which is typically utilized to specify the electron density in present tokamak operation.

D. Plasma resistivity modeling

Following Spitzer resistivity model, the plasma resistivity η is modeled as

$$\eta(\hat{\rho}, t) = \frac{k_{sp}(\hat{\rho})Z_{eff}}{T_e(\hat{\rho}, t)^{3/2}}, \tag{8}$$

where k_{sp} is expressed as

$$k_{sp}(\hat{\rho}) = \frac{\eta(\hat{\rho}, t_{r\eta})T_e(\hat{\rho}, t_{r\eta})^{3/2}}{Z_{eff}}. \tag{9}$$

Note that k_{sp} is evaluated at a reference time $t_{r\eta}$. Z_{eff} is the effective average charge of the ions in the plasma, which is defined as

$$Z_{eff} = \frac{1}{n_e} \sum_{all\ ions} n_j Z_j^2, \tag{10}$$

and where n_j and Z_j denote densities and average atomic numbers of the different ion species.

E. Noninductive current-drive modeling

The total noninductive current-drive [19] is produced by the gyrotron (electron cyclotron) launchers, the neutral beam injectors, and the bootstrap current, and is expressed as

$$\frac{\langle \bar{j}_{NI} \cdot \bar{B} \rangle}{B_{\phi,0}} = \sum_{i=1}^{n_{ec}} \frac{\langle \bar{j}_{ec_i} \cdot \bar{B} \rangle}{B_{\phi,0}} + \sum_{i=1}^{n_{nbi}} \frac{\langle \bar{j}_{nbi_i} \cdot \bar{B} \rangle}{B_{\phi,0}} + \frac{\langle \bar{j}_{bs} \cdot \bar{B} \rangle}{B_{\phi,0}}, \tag{11}$$

where $\bar{j}_{ec_i}$ is the noninductive current generated by the individual gyrotron launchers, n_{ec} is the number of gyrotrons, $\bar{j}_{nbi_i}$ is the noninductive current generated by the individual neutral beam injectors, n_{nbi} is the number of neutral beam injectors, and j_{bs} is the noninductive current generated by the bootstrap effect.

1) Electron cyclotron and neutral beam injection current-drive: Each auxiliary noninductive current-source is modeled as the time varying power in each actuator multiplied by a constant deposition profile in space, which is adequate for a given set of gyrotron launcher and neutral beam injector configurations. The current density provided by each auxiliary source is modeled as

$$\frac{\langle \bar{j}_i \cdot \bar{B} \rangle}{B_{\phi,0}} = k_i(\hat{\rho}) j_i^{dep}(\hat{\rho}) \frac{T_e(\hat{\rho}, t)}{n_e(\hat{\rho}, t)} P_i(t), \tag{12}$$

where $i = [ec_1, \cdots, ec_{n_{ec}}, nbi_1, \cdots, nbi_{n_{nbi}}]$, $k_i(\hat{\rho})$ is a normalizing profile, $j_i^{dep}(\hat{\rho})$ is a reference deposition profile for each current-drive source, and P_i is the power of each current-drive source.

2) Bootstrap current-drive: The bootstrap current arises from the inhomogeneity of the magnetic field strength produced by the external coils in the tokamak, which causes particles in the plasma to become trapped in their orbits around the machine. We write the bootstrap current as

$$\frac{\langle \bar{j}_{bs} \cdot \bar{B} \rangle}{B_{\phi,0}} = \frac{k_{JkeV}R_0}{\hat{F}} \left(\frac{\partial \psi}{\partial \hat{\rho}} \right)^{-1} \left[2L_{31}T_e \frac{\partial n_e}{\partial \hat{\rho}} + (2L_{31} + L_{32} + \alpha L_{34})n_e \frac{\partial T_e}{\partial \hat{\rho}} \right], \tag{13}$$

where we have assumed a tight coupling between the electron and ion species in the plasma (i.e., $T_i \approx T_e$ and $n_i \approx n_e$), k_{JkeV} converts keV into Joule and $L_{31}, L_{32}, L_{34}, \alpha$ are factors that are related to the magnetic configuration of a specified plasma equilibrium and particle collisionality within the plasma [20].

F. Control-oriented model of poloidal magnetic flux profile

By combining the simplified physics-based models for the electron temperature (5) and density (7) profiles, plasma resistivity (8) and, noninductive current-drive $(11) - (13)$ with the magnetic diffusion equation $(3) - (4)$, we obtain a control-oriented model for the poloidal magnetic flux profile evolution. The model can be expressed as

$$\frac{\partial \psi}{\partial t} = f_1(\hat{\rho}, t) \frac{\partial^2 \psi}{\partial \hat{\rho}^2} + \left(\frac{f_1(\hat{\rho}, t)}{\hat{\rho}} + f_2(\hat{\rho}, t) \right) \frac{\partial \psi}{\partial \hat{\rho}} + f_3(\hat{\rho}, t) + f_4(\hat{\rho}, t) \left(\frac{\partial \psi}{\partial \hat{\rho}} \right)^{-1}, \tag{14}$$

with the boundary conditions

$$\left. \frac{\partial \psi}{\partial \hat{\rho}} \right|_{\hat{\rho}=0} = 0 \qquad \left. \frac{\partial \psi}{\partial \hat{\rho}} \right|_{\hat{\rho}=1} = \frac{k}{2} I_p(t), \tag{15}$$

where $k = -\frac{\mu_0}{\pi} \frac{R_0}{\hat{G}(1)\hat{H}(1)}$. The functions f_1, f_2, f_3, f_4 are defined as

$$f_1(\hat{\rho}, t) = \frac{\eta(T_e)D_\psi}{\mu_0 \rho_b^2 \hat{F}^2}, \tag{16}$$

$$f_2(\hat{\rho}, t) = \frac{\eta(T_e)}{\mu_0 \rho_b^2 \hat{F}^2} \left(\frac{\partial D_\psi}{\partial \hat{\rho}} \right), \tag{17}$$

$$f_3(\hat{\rho}, t) = R_0 \hat{H} \eta(T_e) \left(\sum_{i=1}^{n_{ec}} \frac{\langle \bar{j}_{ec_i} \cdot \bar{B} \rangle}{B_{\phi,0}} + \sum_{i=1}^{n_{nbi}} \frac{\langle \bar{j}_{nbi_i} \cdot \bar{B} \rangle}{B_{\phi,0}} \right), \tag{18}$$

$$f_4(\hat{\rho}, t) = R_0 \hat{H} \eta(T_e) \frac{k_{JkeV}R_0}{\hat{F}} \left[2L_{31}T_e \frac{\partial n_e}{\partial \hat{\rho}} + (2L_{31} + L_{32} + \alpha L_{34})n_e \frac{\partial T_e}{\partial \hat{\rho}} \right]. \tag{19}$$

III. Hybrid Numerical Method

A. Discretization in space

A finite difference method is used to discretize the MDE (14)-(15) in space. The spatial grid is defined as

$$\Delta \hat{\rho} = \frac{1}{n-1}, \quad \hat{\rho}_i = (i-1) \cdot \Delta \hat{\rho}, \quad i \in \{1, \cdots, n\}, \tag{20}$$

and the poloidal flux at $\hat{\rho}_i$ can be represented as $\psi_i = \psi(\hat{\rho}_i, t)$. A second order approximation is used for the boundary conditions (15) to obtain conditions for the boundary nodes $\hat{\rho}_1$ and $\hat{\rho}_n$ given by

$$4\psi_2 - \psi_3 - 3\psi_1 = 0, \tag{21}$$

$$4\psi_{n-1} - \psi_{n-2} - 3\psi_n + k\Delta\hat{\rho}I_p(t) = 0. \tag{22}$$

Over the interior nodes $(\hat{\rho}_2, \cdots, \hat{\rho}_{n-1})$, we discretize (14) using also a second order approximation to obtain

$$\dot{\psi}_i = f_1(\hat{\rho}_i, t) \left(\frac{\psi_{i+1} + \psi_{i-1} - 2\psi_i}{\Delta \hat{\rho}^2} \right) +$$
$$\left(\frac{f_1(\hat{\rho}_i, t)}{\hat{\rho}_i} + f_2(\hat{\rho}_i, t) \right) \left(\frac{\psi_{i+1} - \psi_{i-1}}{2\Delta \hat{\rho}} \right) +$$
$$f_3(\hat{\rho}_i, t) + \frac{2f_4(\hat{\rho}_i, t)\Delta \hat{\rho}}{\psi_{i+1} - \psi_{i-1}}. \tag{23}$$

By defining $z = [\psi_2, \psi_3, \cdots, \psi_{n-2}, \psi_{n-1}]^T$, we can express (21)-(23) as

$$\dot{z} = g(z, u), \tag{24}$$

where g is a nonlinear function and

$$u = [\bar{n}_e, P_{ec_1}, \cdots, P_{ec_{n_{ec}}}, P_{nbi_1}, \cdots, P_{nbi_{n_{nbi}}}, I_p]. \tag{25}$$

B. Discretization in time

The temporal grid is chosen as

$$t_j = j\Delta t \quad j \in \{0, 1, \cdots\}, \tag{26}$$

and the poloidal flux at $\hat{\rho}_i$ and t_j is represented as $\psi_{i,j} = \psi(\hat{\rho}_i, t_j)$. At this point a hybrid approach is followed. While the partial derivatives of the parabolic term are evaluated at t_{j+1}, the partial derivative in the interior term coming from the bootstrap-current model together with all the temporal functions are evaluated at t_j, i.e.

$$\frac{\psi_{i,j+1} - \psi_{i,j}}{\Delta t} = f_1(\hat{\rho}_i, t_j) \left(\frac{\psi_{i+1,j+1} + \psi_{i-1,j+1} - 2\psi_{i,j+1}}{\Delta \hat{\rho}^2} \right) +$$
$$\left(\frac{f_1(\hat{\rho}_i, t_j)}{\hat{\rho}_i} + f_2(\hat{\rho}_i, t_j) \right) \left(\frac{\psi_{i+1,j+1} - \psi_{i-1,j+1}}{2\Delta \hat{\rho}} \right) +$$
$$f_3(\hat{\rho}_i, t_j) + \frac{2f_4(\hat{\rho}_i, t_j)\Delta \hat{\rho}}{\psi_{i+1,j} - \psi_{i-1,j}}. \tag{27}$$

By defining $z_j = [\psi_{2,j}, \psi_{3,j}, \cdots, \psi_{n-2,j}, \psi_{n-1,j}]^T$ and evaluating (21) and (22) at t_j, (27) can be written as

$$z_{j+1} = G(z_j, \hat{u}_j) = E_j^{-1} \frac{z_j}{\Delta t} + E_j^{-1} \hat{u}_j, \tag{28}$$

where $E_j = E(t)|_{t=t_j}$, $\hat{u}_j = \hat{u}(t)|_{t=t_j}$, and the matrix $E(t)$ adopts a tridiagonal form.

By evaluating the nonlinear term (last term on the RHS of (23)), which is related to the bootstrap current-drive, at time t_j instead of t_{j+1}, the integration in time of the nonlinear system (24) requires the solution of the tridiagonal system (28) at each instant of time. This hybrid approach, combining both the implicit and explicit methods, reduces the computation complexity allowing for a faster integration while preserving unconditionally stable properties at the expense of a reduced level of accuracy.

IV. OBSERVABILITY OF THE MDE

The observability analysis for the infinite-dimensional system (14)-(15) is beyond the scope of this work. However, the observability analysis for the spatially discretized system is relatively straightforward as it will be shown below.

A. System outputs

Tokamaks without the capability of carrying out MSE-constrained real-time reconstructions of the internal poloidal flux profile still have the capability of providing three related measurements:

1) Poloidal flux at the boundary, $\psi(1, t)$. From (22),

$$\psi_n = \frac{4\psi_{n-1} - \psi_{n-2} + k\Delta \hat{\rho} I_p}{3}. \tag{29}$$

2) Poloidal flux on the magnetic axis, $\psi(0, t)$. From (21),

$$\psi_1 = \frac{4\psi_2 - \psi_3}{3}. \tag{30}$$

3) Total plasma current, $I_p(t)$, given by

$$I_p = -\frac{1}{\mu_0 R_0 \rho_b^2} \int_0^1 \frac{1}{\hat{H}\hat{\rho}} \frac{\partial}{\partial \hat{\rho}} \left(\hat{\rho}\hat{G}\hat{H} \frac{\partial \psi}{\partial \hat{\rho}} \right) \frac{dS}{d\hat{\rho}} d\hat{\rho}, \tag{31}$$

where S denotes the magnetic flux surface.

These three measurements are chosen as the system output,

$$y = \begin{bmatrix} \psi_n & \psi_1 & I_p \end{bmatrix}^T. \tag{32}$$

However, the total plasma current measurement still needs to be expressed as function of the state z. By discretizing (31) in space, it is possible to rewrite (29)-(31) as

$$y = \bar{C}z \triangleq h(z). \tag{33}$$

B. Observability analysis

By combining the state equation (24) with the output equation (33), a nonlinear model is obtained as

$$\begin{aligned} \dot{z} &= g(z, u) \\ y &= h(z) \end{aligned}. \tag{34}$$

By linearizing (34) around a nominal trajectory z^* driven by the nominal input u^*, we obtain

$$\begin{aligned} \delta \dot{z} &= A(t)\delta z + B(t)\delta u \\ \delta y &= \bar{C}\delta z \end{aligned}, \tag{35}$$

where

$$A(t) = \left. \frac{\partial g}{\partial z} \right|_{z^*, u^*}, \qquad B(t) = \left. \frac{\partial g}{\partial u} \right|_{z^*, u^*}, \tag{36}$$

with $\delta z = z - z^*$ and $\delta u = u - u^*$. The Observability Gramian $Q_m(t)$ associated with (35) is defined as

$$Q_m(t_0, t_1) = \int_{t_0}^{t_1} \phi(\tau, t_0)^T \bar{C}(\tau)^T \bar{C}(\tau) \phi(\tau, t_0) d\tau, \tag{37}$$

where ϕ denotes the state transition matrix. The Gramian satisfies

$$\dot{Q}_m(t, t_1) = -A(t)^T Q_m(t, t_1) - Q_m(t, t_1)A(t) - \bar{C}(t)^T \bar{C}(t) \tag{38}$$

with $Q_m(t_1, t_1) = 0$.

While the observability of (34) can be analyzed by examining the rank of the distribution spanned by all repeated Lie derivatives [21], the observability of (35) can by studied by examining the rank of $Q_m(t_0, t_1)$ obtained either from the definition (37) or as the solution of (38). This latter study shows that the system is observable when the output is defined as in (32).
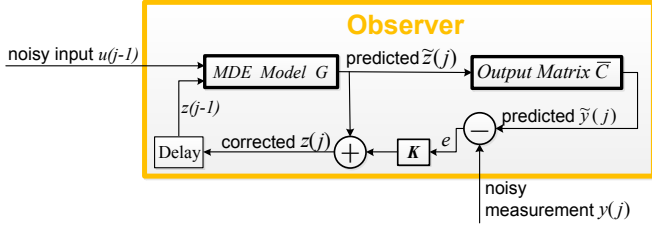
Fig. 2. Observer structure.

V. Observer Design Scheme

By using (28) and (33) we can model our system as a nonlinear discrete lumped-parameter system, i.e.

$$\begin{aligned} z_j &= G(z_{j-1}, \hat{u}_{j-1}) + w_{j-1} \\ y_j &= \bar{C}(z_j) + v_j \end{aligned} \quad . \tag{39}$$

The terms w_j and v_j have been added to account for internal and measurement noise, respectively. They are assumed to be uncorrelated, zero-mean, Gaussian signals, i.e. $w_j \sim N(0, Q_j)$, $v_j \sim N(0, R_j)$, where Q_j and R_j denote their respective covariance matrices. The observer design process based on extended Kalman filtering [22] includes prediction and correction steps as shown in Fig. 2, where $\tilde{z}$ represents the prediction of the state z. The prediction step is given by

$$\tilde{z}_j = G(z_{j-1}, u_{j-1}) \tag{40}$$

$$\tilde{y}_j = \bar{C}(\tilde{z}_j) \tag{41}$$

$$\tilde{P}_j = F_{j-1} P_{j-1} F_{j-1}^T + Q_{j-1} \tag{42}$$

where P is the covariance matrix of z, $F_{j-1} = \frac{\partial G}{\partial z}\big|_{z_{j-1}, u_{j-1}}$. The correction step is given by

$$e_j = y_j - \tilde{y}_j \tag{43}$$

$$K_j = \tilde{P}_j H_j^T (H_j \tilde{P}_j H_j^T + R_j)^{-1} \tag{44}$$

$$z_j = \tilde{z}_j + K_j e_j \tag{45}$$

$$P_j = (I - K_j H_j)\tilde{P}_j \tag{46}$$

where $H_j = \frac{\partial \bar{C}}{\partial z}\big|_{\tilde{z}_j}$.

VI. Analysis of results

Three arbitrary initial profiles for the poloidal magnetic flux have been chosen in order to test the performance of the designed observer, i.e., $\psi_0^1 = 0.4 - 0.1\hat{\rho}^2$, $\psi_0^2 = 0.1 - 0.1\hat{\rho}^2$, $\psi_0^3 = 0.3 - 0.3\hat{\rho}^2$. The grid size is chosen as $\Delta t = 0.02s$ and $\Delta \hat{\rho} = 0.025$. The time span is given by the total length of the discharge in the DIII-D experiments.

Fig. 3 compares the poloidal magnetic flux profiles estimated by the observer with those reconstructed by the real-time equilibrium code (rt-EFIT) [13] in different DIII-D shots. DIII-D has the capability of reconstructing the plasma equilibrium using plasma internal constraints provided by MSE diagnostics, which guarantees a reliable reconstruction of the poloidal magnetic flux profile. As can be seen from the figure, the proposed observer has the potential for reconstructing in real time the poloidal magnetic flux profile in tokamaks without the availability

of MSE diagnostics (or any other diagnostics with the capability of providing plasma internal measurements). Comparisons between rt-EFIT-reconstructed (solid red) and observer-estimated (dashed blue) poloidal magnetic flux profiles from DIII-D shot 147383 are shown in Fig. 3(a), Fig. 3(b), and Fig. 3(c) at different spatial locations. Similar comparison are provided for shot 154358 in Fig. 3(d), Fig. 3(e), and Fig. 3(f), and for shot 147634 in Fig. 3(g), Fig. 3(h), and Fig. 3(i). Fig. 3(j), Fig. 3(k), and Fig. 3(l) compare rt-EFIT-reconstructed and observer-estimated poloidal magnetic flux profiles at time $t = 4.5s$ for DIII-D shots 147383, 154358, and 147634, respectively. All figures also show the estimated profiles obtained just by integrating the MDE equation using the arbitrary initial conditions and the noisy inputs from DIII-D (dashed black). It can be appreciated from the figures that the proposed closed-loop observer is capable of converging to the correct value of the poloidal magnetic flux profile regardless of the initial error and the noise.

VII. Conclusion

A closed-loop observer for the estimation of the poloidal magnetic flux profile has been proposed for tokamaks in which the profile cannot be accurately reconstructed in real time from internal magnetic measurements. The observer has been synthesized by applying extended Kalman filtering theory and using a discrete lumped-parameter nonlinear model of the poloidal magnetic flux profile evolution. This control oriented model is obtained by combining the first-principles MDE with physics-based control-oriented models for the electron temperature, electron density, plasma resistivity and non-inductive current drives. This model has been tailored to high-confinement (H-mode) discharges in the DIII-D tokamak. DIII-D has the capability of accurately reconstructing the poloidal magnetic flux profile by embedding measurements by the MSE diagnostics in the real-time equilibrium code, which makes it a perfect testbed for the proposed observer. Experimental results demonstrates the potential of the proposed observer. The observer makes use of the total plasma current measurement and point-wise measurements of the poloidal magnetic flux at both the magnetic axis and the plasma boundary. Since the observer does not make use of internal measurements of the poloidal magnetic flux profile, it is well suited for tokamaks not provided with internal diagnostics such as the MSE diagnostic.

References

[1] A. Pironti and M. Walker, "Fusion, tokamaks, and plasma control: an introduction and tutorial," *IEEE, Control Systems*, vol. 25, no. 5, pp. 30–43, 2005.

[2] ITER Organization, [Online]. Available: http://www.iter.org.

[3] Y. Ou, C. Xu, and E. Schuster, "Robust Control Design for the Poloidal Magnetic Flux Profile Evolution in the Presence of Model Uncertainties," *IEEE Transactions on Plasma Science*, vol. 38, pp. 375–382, 2010.

[4] Y. Ou, C. Xu, E. Schuster, T. C. Luce, J. R. Ferron, M. L. Walker, and D. A. Humphreys, "Receding-Horizon Optimal Control of the Current Profile Evolution During the Ramp-Up Phase of a Tokamak Discharge," *Control Engineering Practice*, vol. 19, pp. 22–31, 2011.

[5] C. Xu, Y. Ou, and E. Schuster, "Sequential Linear Quadratic Control of Bilinear Parabolic PDEs based on POD Model Reduction," *Automatica*, vol. 47, pp. 418–426, 2011.
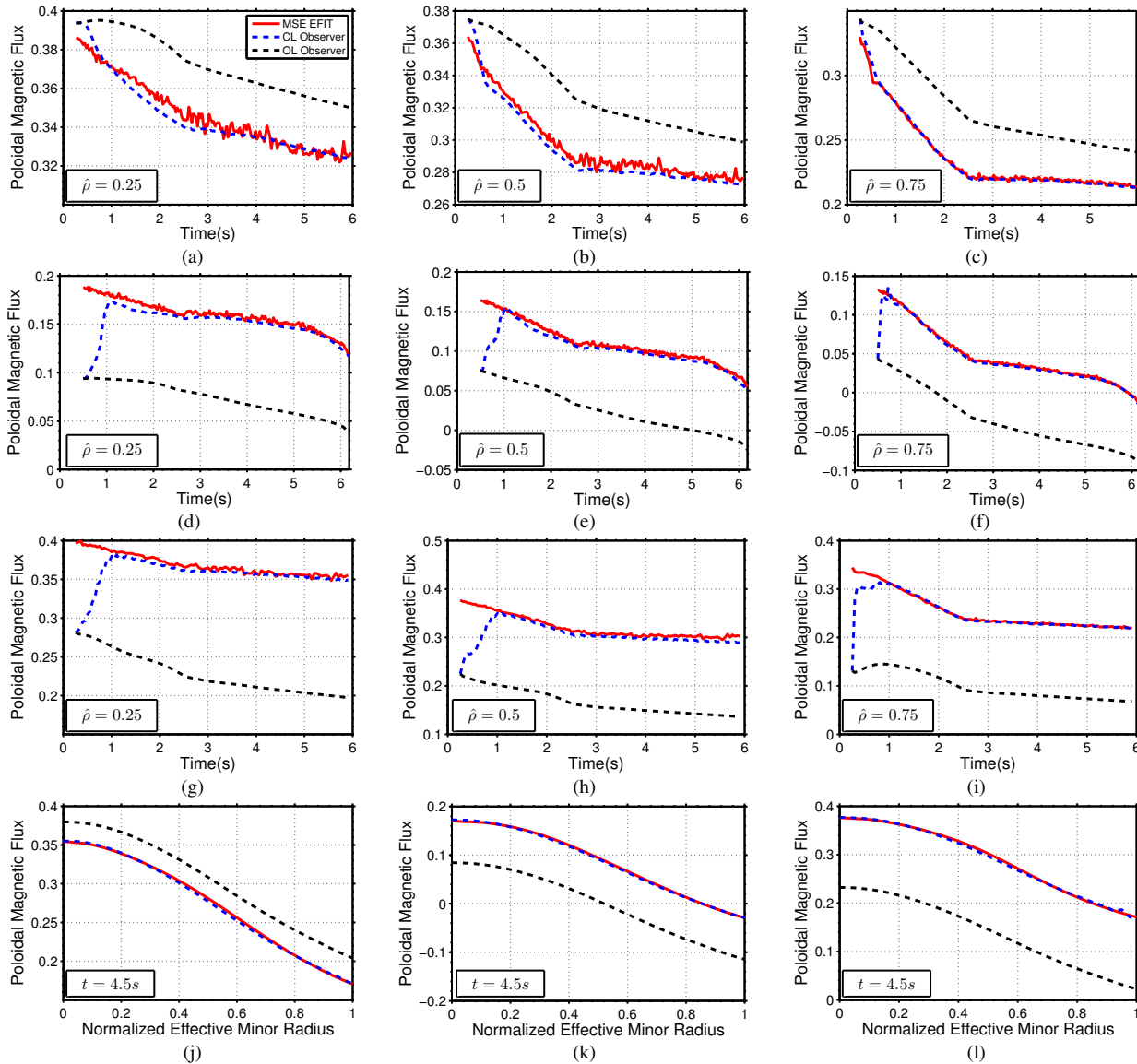
Fig. 3. Actual and estimated poloidal magnetic flux: DIII-D shot 147383 with ψ_0^1 at $\hat{\rho} = 0.25$ (a), $\hat{\rho} = 0.5$ (b), and $\hat{\rho} = 0.75$ (c); DIII-D shot 154358 with ψ_0^2 at $\hat{\rho} = 0.25$ (d), $\hat{\rho} = 0.5$ (e), and $\hat{\rho} = 0.75$ (f); DIII-D shot 147634 with ψ_0^3 at $\hat{\rho} = 0.25$ (g), $\hat{\rho} = 0.5$ (h), $\hat{\rho} = 0.75$ (i); DIII-D shot 147383 with ψ_0^1 at $t = 4.5s$ (j), DIII-D shot 154358 with ψ_0^2 at $t = 4.5s$ (k), DIII-D shot 147634 with ψ_0^3 at $t = 4.5s$ (l).

[6] J. E. Barton, M. Boyer, W. Shi, E. Schuster *et al.*, "Toroidal Current Profile Control During Low Confinement Mode Plasma Discharges in DIII-D via First-principles-driven Model-based Robust Control Synthesis," *Nucl. Fusion*, vol. 52, p. 123018, 2012.

[7] M. D. Boyer, J. E. Barton, E. Schuster *et al.*, "First-principles-driven Model-based Current Profile Control for the DIII-D Tokamak via LQI Optimal Control," *Plas. Phys. Control. Fusion*, vol. 55, p. 105007, 2013.

[8] F. B. Argomedo *et al.*, "Lyapunov-based Distributed Control of the Safety-factor Profile in a Tokamak Plasma," *Nuclear Fusion*, vol. 53, no. 3, p. 033005, 2013.

[9] M. D. Boyer, J. E. Barton, E. Schuster *et al.*, "Backstepping Control of the Toroidal Plasma Current Profile in the DIII-D Tokamak," *IEEE Trans. Control Syst. Technol.*, vol. 22, no. 5, pp. 1725–1739, 2014.

[10] E. Maljaars *et al.*, "Control of the Tokamak Safety Factor Profile with Time-varying Constraints using MPC," *Nuclear Fusion*, vol. 55, p. 023001, 2015.

[11] L. Lao *et al.*, "Reconstruction of current profile parameters and plasma shapes in tokamaks," *Nuclear Fusion*, vol. 25, p. 1611, 1985.

[12] J. Wesson, *Tokamaks*. Oxford, U.K.: Clarendon Press, 1997.

[13] J. Ferron *et al.*, "Real time equilibrium reconstruction for tokamak discharge control," *Nucl. Fusion*, vol. 38, p. 1055, 1998.

[14] D. Hill and the DIII-D Team, "DIII-D research towards resolving key issues for ITER and steady-state tokamaks," *Nuclear Fusion*, vol. 53,

pp. 104 001–18, 2013.

[15] J. E. Barton, W. Shi *et al.*, "Physics-based Control-oriented Modeling of the Safety Factor ProfileDynamics in High Performance Tokamak Plasmas," in *52nd CDC*, 2013, pp. 4182–4187.

[16] Y. Ou, M. L. Walker, E. Schuster, and J. R. Ferron, "Equilibrium Reconstruction Improvement via Kalman-filter-based Vessel Current Estimation at DIII-D," *Fusion Engineering and Design*, vol. 82, pp. 1144–1152, 2007.

[17] C. Xu, Y. Ou, and E. Schuster, "Transport Parameter Estimations of Plasma Transport Dynamics Using the Extended Kalman Filter," *IEEE Transactions on Plasma Science*, vol. 38, pp. 359–364, Mar 2010.

[18] F. Felici, M. de Baar, and M. Steinbuch, "A dynamic state observer for real-time reconstruction of the tokamak plasma profile state and disturbances," in *ACC*, 2014, pp. 4816–4823.

[19] N. J. Fisch, "Theory of current drive in Plasmas," *Reviews of Modern Physics*, vol. 59, no. 1, pp. 200–210, 1987.

[20] O. Sauter *et al.*, "Neoclassical Conductivity and Bootstrap Current Formulas for General Axisymmetric Equilibria and Arbitrary Collisionality Regime," *Physics of Plasmas*, vol. 6, no. 7, p. 2834, 1999.

[21] R. Hermann and A. Krener, "Nonlinear Controllability and Observability," *IEEE Transactions on Automatic Control*, vol. AC-22, no. 5, pp. 728–740, 1977.

[22] B. Anderson and J. Moore, *Optimal Filtering*. Englewood Cliffs, NJ: Prentice-Hall, 1979.